Concurrent optimization of multiple heat transfer surfaces using adjoint-based optimization with a CAD-based parametrization

Pai Raikar, Praharsh; Anand, Nitish; Pini, Matteo; De Servi, Carlo

DOI
10.1016/j.ijheatmasstransfer.2024.126230

Publication date
2025

Document Version
Final published version

Published in
International Journal of Heat and Mass Transfer

International Journal of Heat and Mass Transfer 236 (2025) 126230

Contents lists available at ScienceDirect

International Journal of Heat and Mass Transfer

journal homepage: www.elsevier.com/locate/hmt

Concurrent optimization of multiple heat transfer surfaces using adjoint-based optimization with a CAD-based parametrization

Praharsh Pai Raikar [a,b], Nitish Anand [a], Matteo Pini [b], Carlo De Servi [a,b,*]

[a] Flemish Institute for Technological Research (VITO), Boertang 200, Mol, 3600, Belgium
[b] Delft University of Technology, Kluyverweg 1, Delft, 2629HS, The Netherlands

ARTICLE INFO

Keywords:
Adjoint-based shape optimization
CAD parametrization
Bare-tube heat exchangers
Entropy analysis

ABSTRACT

Heat exchangers are key components of thermal energy conversion systems, however, their optimal design is still based on reduced order models relying on semi-empirical heat transfer correlations. CFD-based design optimization emerged as a viable method to provide a significant improvement in performance at an affordable cost. This study presents a framework to optimize multiple heat transfer surfaces concurrently using the adjoint method. The heat transfer surfaces are parametrized using a CAD-based parametrization method, and their performance is evaluated using a RANS solver complemented by its discrete adjoint counterpart for gradient computation. The optimization framework is applied to minimize the pressure drop across a bare-tube heat exchanger while constraining the heat transfer rate. Two variants of the same optimization problem are formulated: in the first one, the sensitivities are averaged and the tubes are constrained to maintain the same shape, while in the second variant, the shape of the tubes can vary, resulting in an optimum solution with non-identical tube shapes. The results show that the optimized geometry reduces the pressure drop by 19% if the tube shapes are identical, and by 25% in the case of non-identical shapes, compared to the baseline. To identify the physical mechanisms contributing to the fluid-dynamic losses, entropy generation along the flow path was investigated. The results reveal that the major loss reduction observed for the case of non-identical tube shapes is due to the better thermo-hydraulic performance of the first and last tubes.

1. Introduction

Heat exchangers (HEXs) are ubiquitous in thermal energy conversion systems, and they find application in transportation, industrial processes, and residential systems. In aviation, heat exchangers will be the key enabling components of future propulsion and power systems. Examples are condensers of engines enabling carbon-neutral aviation [1], evaporators or condensers in waste-heat recovery systems based on the organic Rankine cycle (ORC) [2], and liquid radiators used to reject low-temperature thermal energy in fuel-cells-based propulsion systems or electric motors/generators [3]. Given that HEXs are arguably the bulkiest components in all these novel technologies, maximizing the thermal-hydraulic performance and reducing their weight and volume is, therefore, decisive to meet the requirement of compactness needed in airborne applications [3].

The standard design practice of heat exchangers is based on reduced order models (e.g., models based on lumped-parameter or one-dimensional methods), making use of correlations based on dimensionless numbers (e.g., the Nusselt number or Colburn factor) for the computation of the heat transfer coefficient and pressure drop [4]. In recent years, parametric studies based on Computational Fluid Dynamics (CFD) have been used to analyze several designs for identifying the optimal HEX geometry [5–12]. These studies investigated the influence of geometric parameters such as tube radius and layout, or fin pitch, thickness, louvered angle, height, and spacing on the performance of the heat exchangers.

Recently, various studies performing shape optimization on heat transfer surfaces have demonstrated the potential of CFD-based automated design methods in improving HEX performance. For example, Ranut et al. [13] optimized the shape of tubular heat exchangers using a multi-objective genetic algorithm (MOGA). The computational cost of the CFD simulation used to evaluate HEX performance was reduced using the streamwise periodic flow approach documented in Ref. [14]. Furthermore, CFD-based meta-models were used to reduce the overall cost of the optimization. Likewise, Bacellar et al. [15] employed Kriging as a surrogate model for reducing the computational expense of CFD-based shape optimization. In the same study, it was established that optimized bare-tube heat exchangers performed better than conventional louvered-fin mini/micro-channel heat exchangers. This paved

* Corresponding author at: Flemish Institute for Technological Research (VITO), Boertang 200, Mol, 3600, Belgium.
E-mail address: carlo.deservi@vito.be (C. De Servi).

https://doi.org/10.1016/j.ijheatmasstransfer.2024.126230
Received 29 April 2024; Received in revised form 26 August 2024; Accepted 15 September 2024
Available online 2 October 2024

the way for further studies on the design of bare-tube HEX [16–18] using the same methodology described in Ref. [15]. Besides optimizing bare-tube HEXs, MOGA has been used to design shell-and-tube HEXs, micro-fins, and heat sinks, utilizing metamodels based on the Kriging method [19–24] and, more recently, neural networks [25,26]. However, surrogate-based methods are suited to handle problems with a limited number of design variables. Therefore, optimizing multiple heat transfer surfaces is unsuitable because of the challenges associated with a larger number of design variables and the computational cost of generating the surrogate models.

For optimization problems characterized by a large number of design variables, gradient-based methods relying on the computation of the sensitivities with the discrete adjoint method are more appropriate [27]. A gradient-based method requires fewer iterations to achieve optimization convergence than a gradient-free method. Furthermore, the discrete adjoint method enables the calculation of gradients of objective functions that require the solution of RANS equations at a cost similar to that of the flow solver, irrespective of the number of design variables. Shape optimization based on the adjoint method has been recently applied to the automated design of heat transfer elements, in combination with different geometry parametrization techniques. Zhang and Qian [28] performed a parametrization-free shape optimization of multiple fins, in which the design variables were the mesh nodes of the design surfaces. The optimized fins provided a 75% increase in the outlet temperature for the same pressure drop of the baseline design. Wang et al. [29] utilized the adjoint method for parametrization-free 3D shape optimization of fins in recuperators of Brayton power cycles using supercritical carbon dioxide. The computational domain was simplified to include only a single fin per cold and hot sides, and the design variables were the nodes of the fin surface mesh. A method used to parametrize the HEX geometry is through the so-called free-form deformation (FFD) boxes. Anibal et al. [30] employed FFD for optimizing novel heat sinks for the thermal management of electric motors in aerospace applications. In more recent work, Anibal and Martins [31] applied the same optimization framework to optimize plate-fin heat exchangers for aerospace applications with the objective of minimizing drag and weight. FFD boxes based on volumetric B-splines offer better control on the geometry than conventional FFD and parameter-free approaches. Gkaragkounis et al. [32] performed a multi-objective shape optimization of 3D fins to obtain a Pareto front with respect to two objective functions: the minimization of pressure losses and the maximization of the heat transfer rate. Albeit FFD boxes can be used to parametrize arbitrarily complex shapes, they are not suited for imposing the geometric constraints that are needed to guarantee that the optimal geometry can eventually be manufactured [33,34]. Conversely, a CAD-based parametrization of the design surface, defined by NURBS control points, provides a much better definition of the design surface and a complete control over it [35,36]. Constrained optimization with CAD-based parametrization has been successfully applied for the optimal design of turbomachinery blades. For example, Xu et al. [36] applied CAD-based parametrization to the optimization of a one-stage turbine with geometric constraints on blade thickness and trailing edge radius. Agromayor et al. [37] developed a CAD-based blade parametrization method suitable for axial and radial turbomachines that was used to perform adjoint-based shape optimization with the open-source software SU2 [38,39]. Châtel and Verstraete [40] utilized a CAD-based parametrization along with the discrete adjoint method to perform constrained aero-structural optimization of a radial compressor.

Application of adjoint-based shape optimization with the CAD representation of the design surface embedded in the automated design chain has been mostly confined to the design of single geometries, and studies dealing with the concurrent design of multiple surfaces remain limited: Gkaragkounis et al. [41] optimized a 2D representation of the internal cooling channels of a gas turbine blade, though only the blade profile and the location of the cooling channels were varied. This study aims to establish a methodology to perform adjoint-based shape optimization of multiple heat transfer surfaces using CAD-based parametrization. An automated design chain developed for this purpose encompasses the open-source CFD suite SU2 [38] – to perform CFD simulations, adjoint evaluations, and mesh deformation – and a python-based CAD parametrization tool [37,42] – to parametrize the heat transfer surfaces using NURBS. The design chain is applied to the optimization of an array of two-dimensional tubes, representing a simplified configuration of a bare-tube heat exchanger, as described in Ref. [15]. Two optimization problems are formulated: one in which the sensitivities are averaged to impose the same shape deformation to the various tubes, and the other in which the tubes are concurrently optimized, albeit independently. The optimized designs are compared to the baseline case in terms of flow and heat transfer characteristics. Entropy generation along the flow path is finally investigated to identify the physical mechanisms contributing to loss.

2. Methodology

The optimization framework encompasses the open-source CFD software SU2 [38] embedding a discrete adjoint method for gradient calculation, a solver for mesh deformation, a CAD-based parametrization tool [37,42], and a gradient-based optimizer.

The overall optimization framework is illustrated by means of the XDSM diagram shown in Fig. 1. The heat transfer design surfaces, such as heat exchanger tubes or fins, are parametrized through curves controlled by a set of design variables ($\boldsymbol{\alpha}$). At each design iteration, the surface coordinates $\left(\mathbf{X}_{\text{surf}}\right)$ defined by the parametric curves, are generated. The corresponding volume mesh $\left(\mathbf{X}_{\text{vol}}\right)$ is obtained by deforming the initial mesh. The value of the objective function (J) and the flow-related constraints (c_{f}), like the heat transfer rate $\dot{Q}$, are then computed with SU2. Next, the gradients of the cost functions with respect to the mesh coordinates $\left(\frac{\mathrm{d}J}{\mathrm{d}\mathbf{X}_{\text{vol}}}, \frac{\mathrm{d}c_{\text{f}}}{\mathrm{d}\mathbf{X}_{\text{vol}}}\right)$, are computed using the adjoint solver. Finally, the gradient values of the cost functions with respect to the design variables ($\boldsymbol{\alpha}$) are obtained by applying the chain rule of differentiation. The sensitivity of the objective function with respect to the design variables can be therefore written as

$$\frac{\mathrm{d}J}{\mathrm{d}\boldsymbol{\alpha}} = \frac{\mathrm{d}J}{\mathrm{d}\mathbf{X}_{\text{vol}}} \cdot \frac{\mathrm{d}\mathbf{X}_{\text{vol}}}{\mathrm{d}\mathbf{X}_{\text{surf}}} \cdot \frac{\mathrm{d}\mathbf{X}_{\text{surf}}}{\mathrm{d}\boldsymbol{\alpha}}, \tag{1}$$

where $\frac{\mathrm{d}\mathbf{X}_{\text{vol}}}{\mathrm{d}\mathbf{X}_{\text{surf}}}$ is the sensitivity of the mesh coordinates with respect to the mesh nodes of design surfaces and $\frac{\mathrm{d}\mathbf{X}_{\text{surf}}}{\mathrm{d}\boldsymbol{\alpha}}$ represents the sensitivity of the mesh nodes of the design surfaces with respect to the design variables. The methods underlying the various blocks of the optimization framework illustrated in Fig. 1 are presented in the following.

2.1. Optimizer

The gradient-based optimization method Sparse Nonlinear OPTimizer (SNOPT) [43], interfaced by means of the open-source python package *pyOptSparse* [44], is adopted. SNOPT is suited for constrained shape optimization problems involving multiple design surfaces because of its advantages in handling large-scale problems with sparse matrices.

2.2. Geometry modeler

The heat transfer design surfaces are constructed using the CAD-based parametrization method from Ref. [37]. This method facilitates the parametrization of a broad range of geometries of HEX tubes and fins, ranging from conventional shapes, such as circular and elliptical, to more unconventional designs, such as tear-drop and airfoil-type geometries, also in the case of 3D features. For 2D geometries, each design surface is represented by three NURBS curves: the camberline, the upper side, and the lower side, as shown in Fig. 2. The upper and

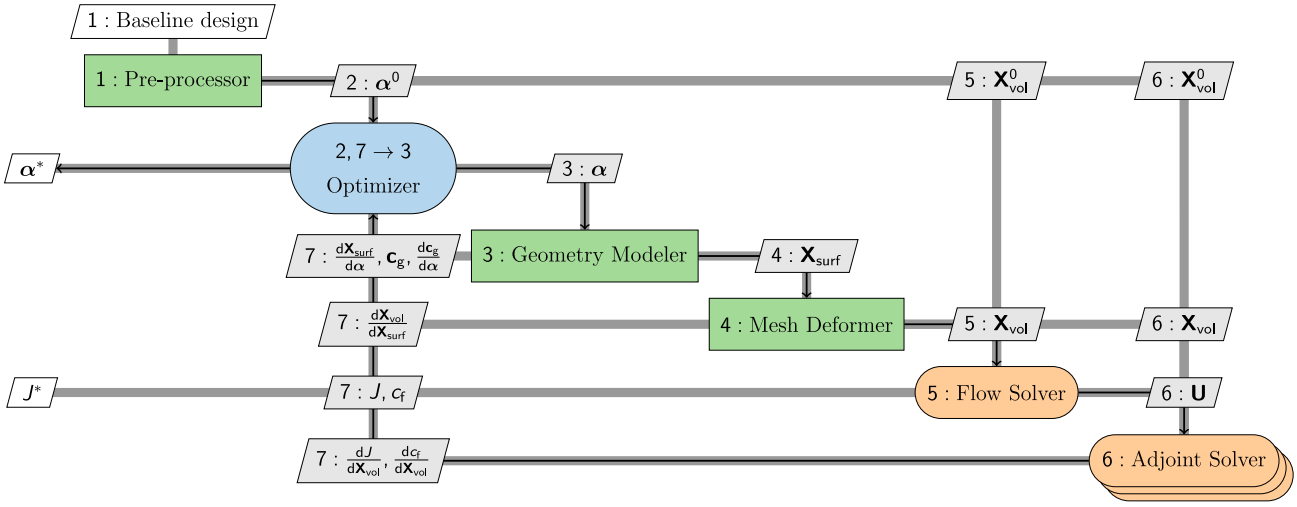

Fig. 1. XDSM diagram depicting the inter-dependencies among the blocks of the optimization framework.

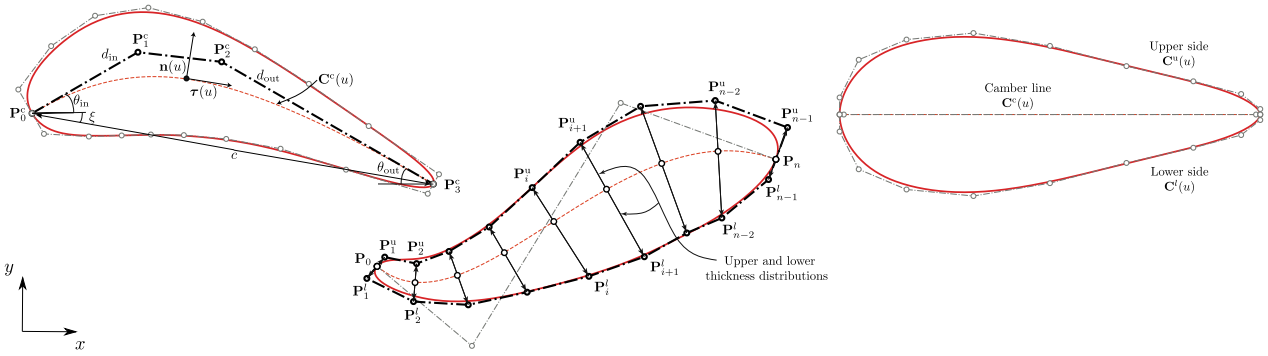

Fig. 2. Construction of multiple 2D geometries using the camber line-thickness approach. The three design surfaces (in red) demonstrate the application of the main three steps of the parametrization procedure, though to different HEX fins/tube shapes. In the first geometry (left), the parameters defining the camber line are highlighted. The middle geometry demonstrates how the thickness distributions are applied around the camber line, while in the final geometry (right), the NURBS curves representing the complete design surface are annotated. (For interpretation of the references to color in this figure legend, the reader is referred to the web version of this article.)

the lower sides are generated by imposing thickness distributions on the camberline, see Fig. 2. The camberline is defined as a cubic B-spline curve, while the upper and lower sides are B-spline curves of fourth order. These curves are defined by the design variables tabulated in Table 1, and the equations describing them are documented in Ref. [37]. In the case of 3D geometries, the camber surface is defined using a bi-quartic B-spline. Similarly, the upper and lower sides of the 3D geometry are defined using B-spline surfaces of fourth order.

The sensitivities of the design surfaces with respect to the design variables, namely the CAD sensitivities $\left(\frac{d\mathbf{X}_{\text{surf}}}{d\alpha}\right)$, are computed using the complex-step method [45] that guarantees second-order accuracy. Thanks to the CAD parametrization, arbitrary geometric constraints ($\mathbf{c}_g$) and their sensitivities $\left(\frac{d\mathbf{c}_g}{d\alpha}\right)$ can be directly computed differentiating the NURBS curves.

2.3. Mesh deformer

Mesh deformation is performed using the linear elasticity equations [46] in which the surface deformation is imposed as a Dirichlet boundary condition. This method, available within SU2, has been proven efficient and robust to handle the deformation of complex meshes. However, for large deformations, the mesh quality may be compromised.

2.4. Flow solver

Incompressible RANS simulations are performed using SU2 [38, 47] to assess the thermal-hydraulic performance of HEXs. The discretized form of the RANS equations is obtained using a finite volume method, in which the convective fluxes are reconstructed with the Flux-Difference-Splitting (FDS) method [48], and the MUSCL [49] approach is used to achieve second-order accuracy. The spatial gradients are computed using the Green–Gauss [50] method. The turbulence effects are modeled with the Spalart–Allmaras [51] model, and full resolution of the boundary layer is achieved by prescribing $y^+ < 1$ at the heat transfer surfaces. The steady-state solution is achieved using a time-marching scheme with Euler implicit time integration. Overall, the linearized governing equations are solved using the flexible generalized minimum residual (FGMRES) method [52] with an ILU preconditioner.

2.5. Adjoint solver

The sensitivities of the cost functions with respect to the mesh coordinates $\left(\frac{dJ}{d\mathbf{X}_{\text{vol}}}, \frac{dc_f}{d\mathbf{X}_{\text{vol}}}\right)$ are computed using the discrete adjoint method, and the numerical derivatives are obtained by means of the reverse mode of the open-source algorithmic differentiation tool CoDiPack

Table 1
Design variables for the 2D camberline-thickness parametrization.

Variable name	Symbol(s)
Leading edge abscissa and ordinate	x_{in}, y_{in}
Axial chord length	c_{ax}
Stagger angle	ξ
Inlet and exit metal angles	$\theta_{in}, \theta_{out}$
Inlet and exit tangent proportions	d_{in}, d_{out}
Inlet and exit radii of curvature	r_{in}, r_{out}
Upper and lower thickness distributions	t^u, t^l

[53], available within SU2. The formulation of the adjoint equations and their implementation in SU2 are documented in Ref. [54]. The discretization schemes used for the adjoint equations are the same as those used for the flow equations.

2.6. Sensitivity computation for optimization of multiple heat transfer surfaces

Multiple design surfaces are represented by a consistent parametrization method (CP), i.e., a method exploiting the same set of CAD parameters for each surface. This choice implies that the CAD parameters of a HEX configuration with identical pins or tubes are the same for all surfaces, apart from the leading edge coordinates. When concurrently optimizing multiple surfaces, the design sensitivities of the various surfaces typically differ due to the varying local flow conditions. Therefore, it can be hypothesized that performing shape optimization in which each heat transfer surface is separately optimized can provide significantly improved HEX performance. In order to verify such a hypothesis, two formulations of the same optimization problem are conceived, termed consistent parametrization with local sensitivities (CP-LS) and consistent parametrization with averaged sensitivities (CP-AS). In the CP-LS formulation, each geometry is optimized independently from the others, in accordance with the computed values of the gradient. Conversely, in the CP-AS, the sensitivities of the cost functions are averaged, yielding to

$$\frac{\mathrm{d}f}{\mathrm{d}\boldsymbol{\alpha}_i} = \frac{1}{N}\sum_{j=1}^{N}\frac{\mathrm{d}f}{\mathrm{d}\boldsymbol{\alpha}_i^j}, \tag{2}$$

where f is the cost function, i indicates the design variable, N is the total number of design surfaces, and j denotes the design surface. Note that, with this method, identical shapes are obtained if the initial HEX configuration features the same geometry of pins or tubes.

Additionally, sensitivity averaging is performed to prevent asymmetric tube shapes during the optimization due to numerical inaccuracies and discretization errors. To this purpose, the sensitivities corresponding to the design variables of the upper and lower thickness distributions are averaged using the following equation

$$\frac{\mathrm{d}f}{\mathrm{d}\boldsymbol{\alpha}_i} = \frac{1}{2}\left(\frac{\mathrm{d}f}{\mathrm{d}\boldsymbol{\alpha}_i^u} + \frac{\mathrm{d}f}{\mathrm{d}\boldsymbol{\alpha}_i^l}\right) \tag{3}$$

where i is the index of the design variable in the thickness distribution array, and superscripts u, l indicate the upper and lower surface of the tube.

3. Case study

3.1. Tubular heat exchanger geometry

The optimization framework is applied to a bare-tube air-to-fluid heat exchanger configuration. Bare tube heat exchangers, used as radiators, evaporators, and condensers, are promising in automotive and aerospace applications because of their lower weight and pressure drop compared to the conventional mini/micro-channel HEX [15,16]. The focus in this case study is on improving the air-side performance of such HEX given that their design is largely driven by the heat transfer and pressure losses in the airflow. The test case is inspired by the bare-tube radiator in Ref. [15] for which experimental data is available. The tubes are arranged in a staggered layout, resulting in a design that delivers a heat load comparable to that of conventional mini/micro-channel HEX while having a lower air-side pressure drop. The geometry arrangement consists of 7 ranks of tubes in the streamwise direction, as shown in Fig. 3, while Table 2 presents the dimensions of the baseline geometry.

Table 2
Parameters defining the tube bundle configuration of the case study.

Design variable	Description	Value [$\times 10^{-3}$ m]
h_t	Height	1.1
w_t	Width	3.0
δ_t	Thickness	0.3
P_l	Longitudinal tube pitch	2.4
P_t	Transverse tube pitch	2.2
d	HEX width	17.4

Table 3
Thermo-physical properties of air at 313 K.

Density (ρ) [kg/m^3]	Specific heat (C_p) [J/(kg K)]	Viscosity (μ) [Pa s]	Thermal conductivity (k) [W/(m K)]
1.1275	1006.9	1.9148×10^{-5}	0.0271

3.2. Numerical model

Since the case study focuses on improving the hydraulic performance of the air-side of the radiator and the temperature change of the working fluid inside the tubes is much lower than that of the airflow, isothermal wall boundary conditions are applied on the external surface of the tubes. Fig. 4 depicts the computational domain with the boundary markers. The inflow ($1w_t$) and outflow ($3w_t$) boundaries of the domain were placed sufficiently far from the tubes to avoid any flow disturbance.

The boundary conditions for this case study correspond to an air volume flow rate of 0.03 m^3/s. A velocity of 3 m/s and a temperature of 300 K were prescribed at the inlet. The free-stream turbulence intensity at the inlet was 5%, and the turbulent to laminar viscosity ratio was 10. The atmospheric pressure value was imposed on the outlet boundary by setting a gauge pressure value of 0 Pa, while the top and bottom boundaries were set as periodic boundaries. At the tube walls, a constant temperature of 350 K and no-slip boundary conditions were imposed. Overall, the test case is characterized by a Reynolds number of 530 by taking as characteristic length the major axis of the tube and as velocity the free-stream velocity. In all simulations, the fluid properties were assumed to be constant. Table 3 shows the values of the fluid properties at ambient pressure and a temperature of 313 K, which is approximately the average temperature value in the computational domain.

The flow around the tube bundle was solved by means of RANS equations using the numerical schemes described in Section 2.4. A CFL number of 10 was selected for the optimization study to ensure the stability of the convergence process. The maximum number of iterations per cycle of the FGMRES linear solver was set to 10 with a convergence tolerance of 10^{-4}. The flow simulations were terminated once the residuals of the governing equations were reduced by 5 orders of magnitude.

3.3. Grid independence study and model verification

The variation of the performance parameters – pressure drop and heat transfer rate – with mesh density was investigated. For this purpose, five unstructured hybrid meshes were generated using a commercial meshing tool [55]. The meshes comprise quadrilateral elements

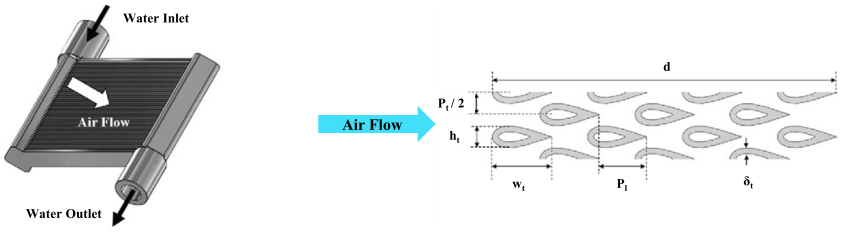

Fig. 3. Illustration of tubular heat exchanger geometry from Ref. [15].

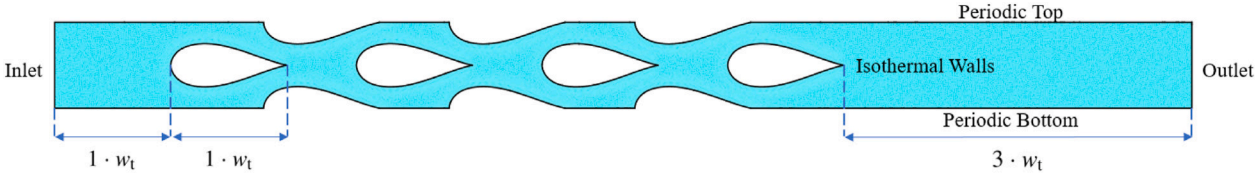

Fig. 4. Computational domain (with boundary markers) corresponding to the baseline design of the selected test case.

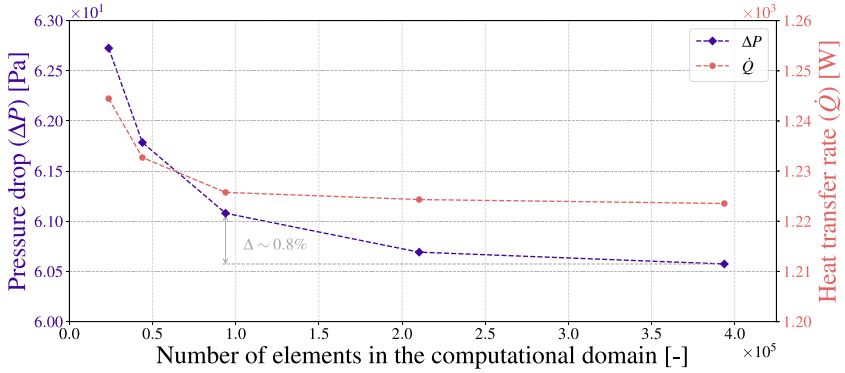

Fig. 5. Variation of performance parameters with mesh density.

around the walls and triangular elements in the rest of the domain, see Fig. 6. The mesh refinement strategy was such that the average element size was halved while the inflation layer thickness and progression were kept consistent across the different meshes. This was done to cluster the mesh cells to guarantee y^+ values less than 1 close to walls.

The air-side pressure drop in the heat exchanger was estimated from the pressure difference between the inlet and the outlet in the computational domain using Eq. (4), while the heat transfer rate of the heat exchanger was calculated from the average temperature increase from the inlet to the outlet using Eq. (5). The variation of the estimated pressure drop and heat transfer rate with the mesh density is shown in Fig. 5, where a monotonic convergence of both quantities can be observed. For the purpose of the study, the mesh with about 94,000 elements was selected (shown in Fig. 6) as the deviations of pressure drop and heat transfer rate compared to the finest mesh are approximately 0.8% and 0.2%, respectively.

$$\Delta P_{\text{air}} = P_{\text{in}} - P_{\text{out}}. \tag{4}$$

$$\dot{Q} = \dot{m} C_{\text{p}} (T_{\text{out}} - T_{\text{in}}). \tag{5}$$

Furthermore, comparing the simulation output using the selected mesh to the experimental and numerical results published in Ref. [15], it was observed that the pressure drop was under-predicted by about 1.5% and 5%, respectively. Conversely, the heat transfer coefficient was over-predicted by roughly 7.5% and 2%. These discrepancies are relatively low, and they can be attributed to measurement uncertainty as well as the choice of the turbulence model, the assumption of constant air properties, and differences in the numerical setup. It can be concluded that the CFD model is reliable for the application at hand.

3.4. Optimization problem

The objective of the optimization is to minimize the pressure drop across the heat exchanger while maintaining a minimum required heat transfer rate. The mathematical formulation of the optimization problem is as follows

$$\min_{\boldsymbol{\alpha}} \quad \Delta P_{\text{air}}(\boldsymbol{\alpha}), \tag{6}$$

$$\text{subject to} \quad \dot{Q} \geq \dot{Q}_0, \tag{7}$$

$$a \geq a_0, \tag{8}$$

where $\boldsymbol{\alpha}$ represents the design variables, ΔP_{air} is the air-side pressure drop, $\dot{Q}$ is the heat transfer rate (computed using Eq. (5)), $\dot{Q}_0$ is the heat transfer rate of the baseline design, a is the area enclosed within each tube and a_0 is the area enclosed within each tube of the baseline geometry. Such area constraint is specified to prevent the pressure drop of the fluid flowing within the tubes (not modeled) from deviating significantly from that of the baseline geometry. A tolerance of 1.5% and 0.5% is assigned to the values of the heat transfer and area constraint to improve the robustness of the optimization.

Two variants of the optimization problem are formulated, which differ in the method adopted for sensitivity computation as described in Section 2.6. The first setup utilizes the CP-AS method, which results in tubes of identical shapes, while the second one adopts the CP-LS method, resulting in non-identical tube configurations.

3.4.1. Design variables

The design variables are the CAD parameters defining the upper and lower thickness distributions around the camberline. As the tubes

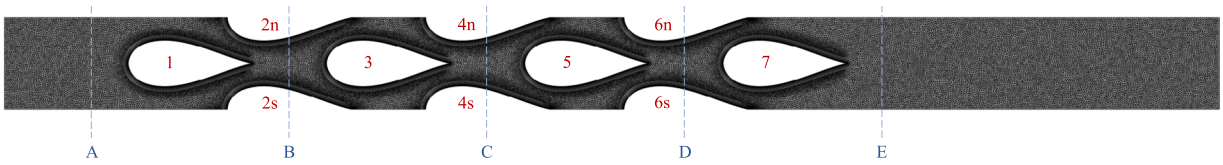

(a) Entire domain with labels for the tube design surfaces and lines at which the flow field is analyzed

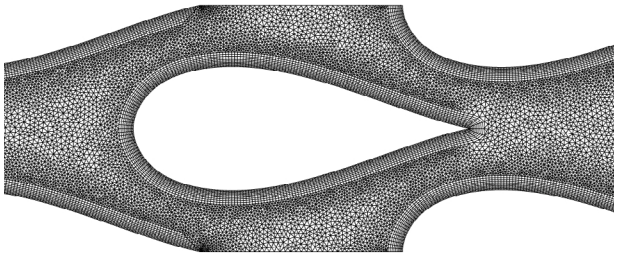

(b) Enlarged view of the mesh

Fig. 6. Discretized flow domain selected from the grid independence study.

Table 4
Thickness values for the upper and lower profile of the baseline tube geometry (identical for all tubes).

Design variable ($t_i^{u/l}$)	Thickness [m]
t_1	3.284×10^{-4}
t_2	2.910×10^{-4}
t_3	5.204×10^{-4}
t_4	6.432×10^{-4}
t_5	3.468×10^{-4}
t_6	3.268×10^{-5}
t_7	1.000×10^{-9}
t_8	6.391×10^{-6}

are symmetric with respect to the main axis, each design surface is described by eight independent parameters $t_i^{u/l,j}$ where i denotes the parameter index in the upper/lower distribution array and j denotes the tube number as per the labels shown in Fig. 6(a). The values of the design variables corresponding to the baseline configuration are listed in Table 4. Bounds are imposed on the design variables to avoid unfeasible shapes and issues related to the intersection of the tube surfaces.

3.4.2. Constraints

The geometric constraint imposed on the tube cross-section is computed using the shoelace formula [56]. According to this formula, for a given set of p vertices (x_i, y_i) of any non-intersecting polygon, ordered in a clockwise or counterclockwise manner, the area a can be computed as:

$$a = \frac{1}{2}\left|\sum_{i=1}^{p-1}(x_i y_{i+1} + x_p y_1) - \sum_{i=1}^{p-1}(y_i x_{i+1} + y_p x_1)\right|. \tag{9}$$

By this method, the area enclosed within a polygon is computed by the sum of the area of the triangles formed by the origin with two vertices of the polygon in a sequential order. Fig. 7 illustrates the area calculation method for an arbitrary polygon with ten vertices arranged in the counterclockwise direction. The sensitivities of the area constraint with respect to the design variables are computed using the complex-step method.

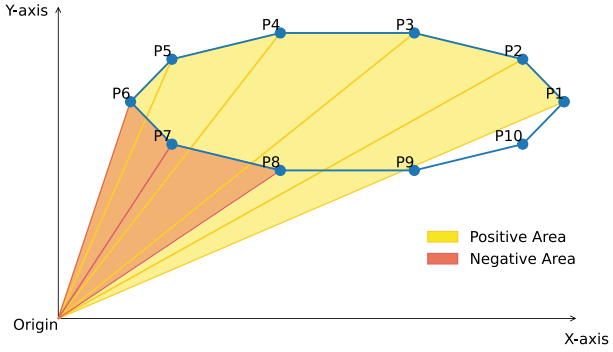

Fig. 7. Illustration of the use of the shoelace method for calculating area of 2-D enclosed polygon.

4. Results

4.1. Gradient verification

To verify the gradient values obtained using the adjoint (ADJ) method, they are compared to those computed using the finite difference (FD) method. The step sizes chosen for the finite difference method were 0.05% and 0.01% for the cost functions of pressure drop and heat transfer rate, respectively. These values of step sizes were chosen after performing a parametric analysis. The value of the gradients of both the pressure drop and heat transfer rate with respect to the design variables $\left(\frac{df}{d\alpha}\right)$ computed with the two methods are displayed in Fig. 8.

As seen from Fig. 8, the gradient values for the cost functions computed by the adjoint method are quantitatively in agreement with those computed by the finite difference method. An average deviation of less than 5% was obtained for all the design variables, apart from $t_7^{u/l,j}$. For the chosen step size, the design variables $t_7^{u/l,j}$ show the largest discrepancies as their values are orders of magnitude smaller than the other design variables (see Table 4). Increasing the step size of the FD method would reduce the discrepancy observed for $t_7^{u/l,j}$, but will affect the gradient estimation for the other variables. Overall, the gradients obtained using the design chain are deemed sufficiently accurate for the optimization study.

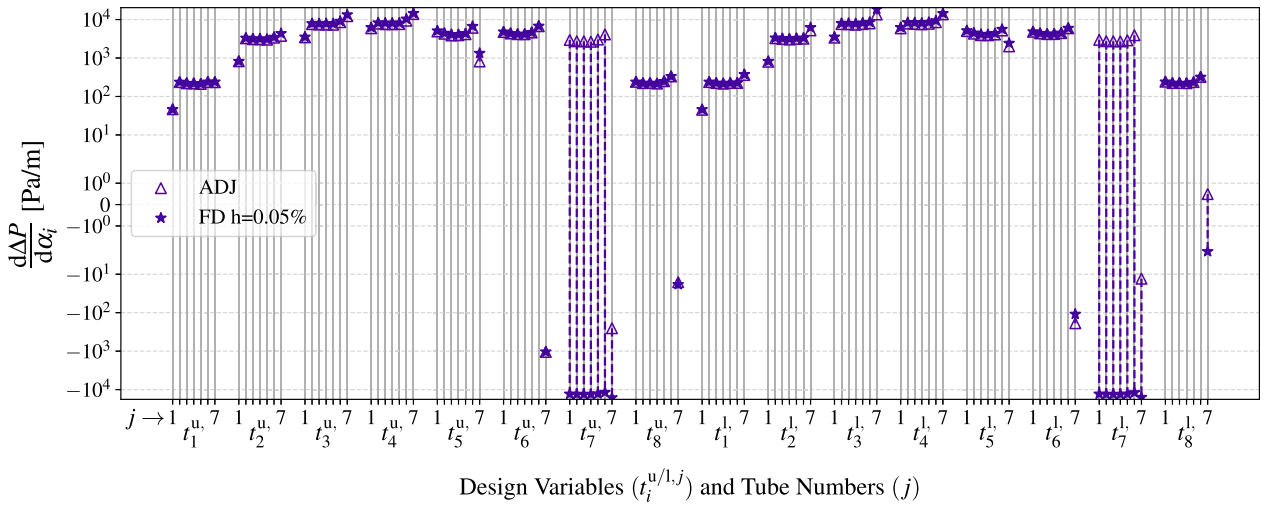

(a) Pressure drop

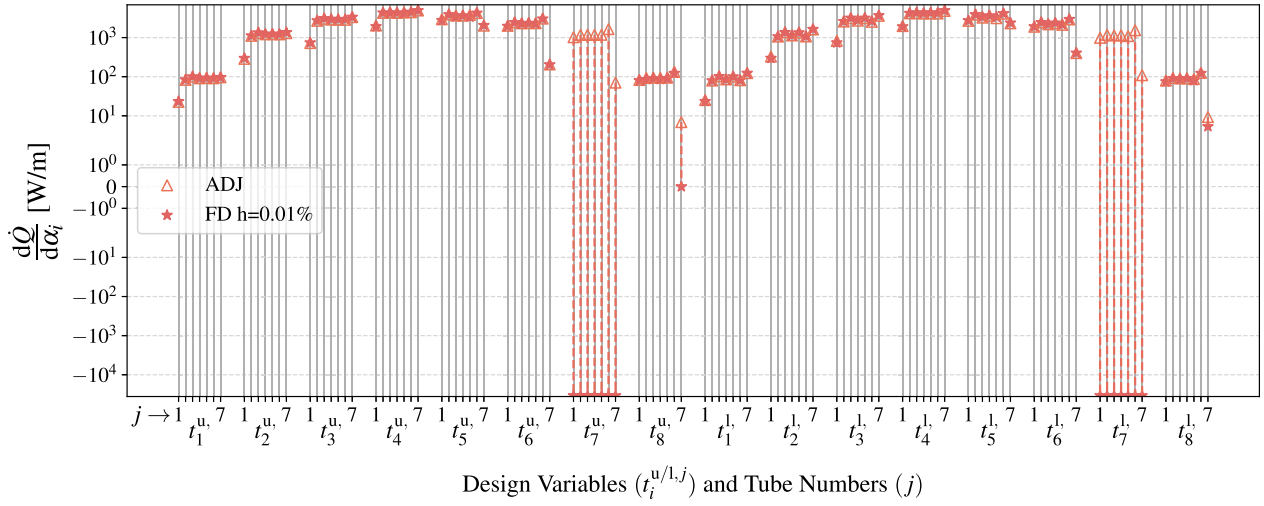

(b) Heat transfer rate

Fig. 8. Gradient verification plots for the cost functions in the optimization case study.

4.2. Optimization results

The optimization results are presented for the two cases described earlier in Section 3: identical (CP-AS) and non-identical tubes (CP-LS). The plots in Fig. 9 illustrate the convergence trend of the optimization problem. Both the objective function and the constraints are displayed. As can be observed, for the case with identical tubes, a 19.41% performance improvement is achieved in 11 design iterations. In the second case, instead, a reduction of total pressure loss of about 25% is obtained in 19 design iterations. The computational time required for each flow and adjoint simulation was ~10 min on a workstation with *Intel Xeon Gold 5220R* (2.2 GHz) processor having 192 GB memory. The case with identical tubes leads to a faster optimization convergence due to fewer distinct design variables as a result of the sensitivity averaging. Furthermore, Fig. 9 illustrates that the optimum design in the identical tubes case achieves a heat transfer rate about 0.5% lower than the baseline design, thereby not fully utilizing the allowed tolerance of about 1.5%. In both cases, however, the prescribed constraints on the heat transfer rate and the area enclosed within the tubes are satisfied by the optimization process. Thus, the pumping losses are reduced while maintaining the required heat transfer rate.

Fig. 10 shows the baseline and optimal tube bundle configurations. Compared to the prominently front-loaded tube shapes in the baseline design, the optimum solution with identical tubes exhibits a slender profile, leading to a more aerodynamic shape. In the non-identical tube case, a similar pattern is obtained for the shapes of tubes 2–6 (see tube labels in Fig. 6(a)). Tubes 1 and 7 have different shapes, accounting for the local flow conditions, namely the entrance and exit effects for the tube bundle.

Fig. 11 illustrates the variation of the normalized flow passage area in the streamwise direction for the three designs. As seen from Fig. 11, the baseline design features a higher metal blockage, which induces higher velocity peaks, thus higher fluid-dynamic losses. The more significant geometrical differences between the two optimal designs are related to the geometry of the last tube, in particular, the slender profile of the last tube (Tube 7) featured in the non-identical configuration guarantees a more gradual flow diffusion process downstream of the tube bundle.

The contours of the flow properties – velocity, pressure, and temperature – for the three designs are shown in Fig. 12. The velocity contours (see Fig. 12(b)) substantiate the trends observed by the area-variation plot in Fig. 11. The baseline design has higher velocities in

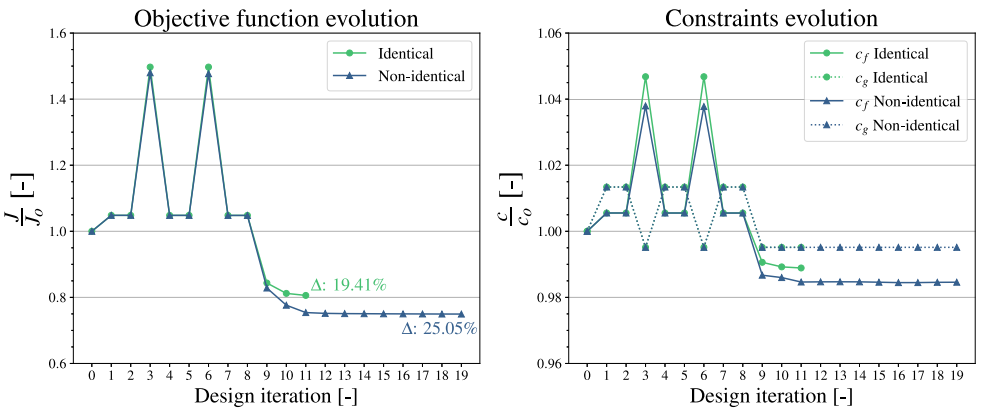

Fig. 9. Optimization history plots depicting the evolution of cost functions with design iterations.

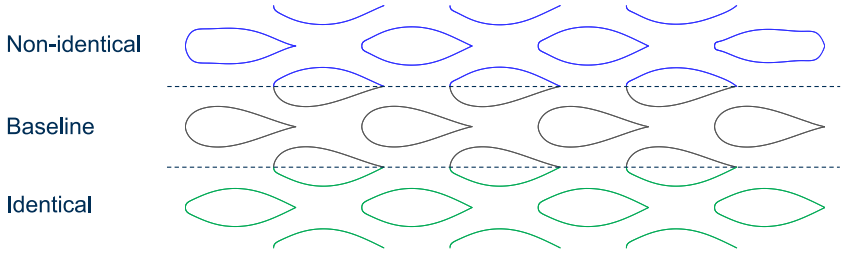

Fig. 10. Comparison of the baseline tube bundle geometry with optimum designs having identical and non-identical tubes.

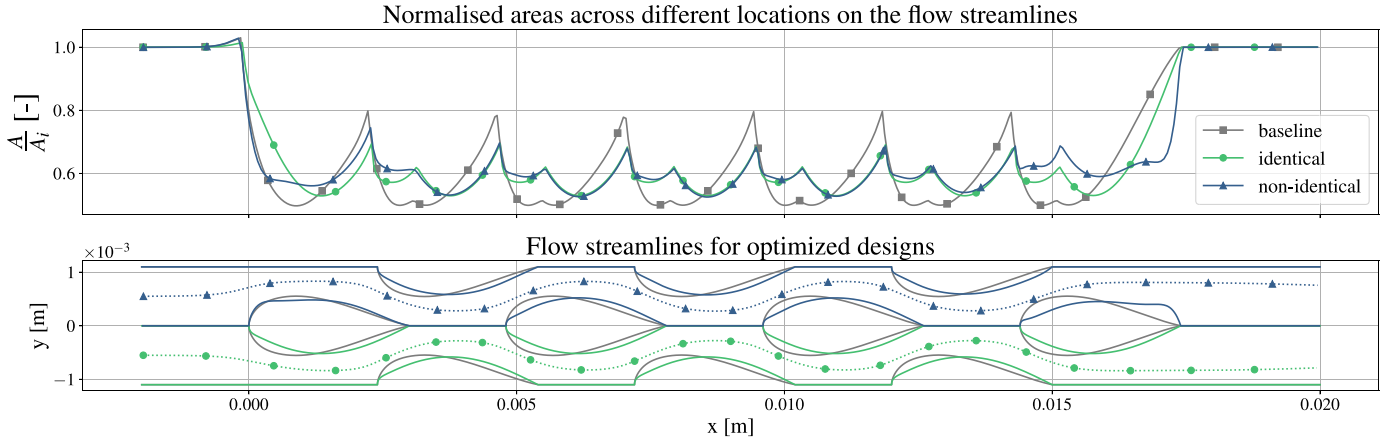

Fig. 11. Comparison of the normalized flow passage area variation between the baseline design and the optimum designs having identical and non-identical tubes.

the flow region between the end of a tube row and the leading edge of the following one compared to the optimum designs. Comparing the local velocities around the upstream half of Tube 7, it can be observed that the local velocity magnitudes are the lowest for the non-identical design. Moreover, the gradual increase of the tube thickness for the optimum designs eliminates the region of adverse pressure gradient observed in the baseline design due to the large curvature at the leading edge for the baseline tube shapes. Fig. 12(a) depicts the pressure contours for the three designs where the flow stagnation regions can be qualitatively noted. The temperature contours for the designs are shown in Fig. 12(c). Qualitatively the three different tube geometries result in similar temperature contours, as the heat transfer rate is constrained along with the internal area for each tube.

Furthermore, the flow properties are sampled at various locations along the streamlines as well as the tube surfaces. Fig. 13 shows the flow properties – velocity, pressure, and temperature – at the locations A to E (see Fig. 6(a)) in the flow domain. All the locations are equidistant from one another and locations B, C, and D are located at half of the chord length of the tubes 2, 4 and 6, respectively. As observed in the plots of the velocity field, the maximum observed velocity is reached at location D. The maximum velocity is the highest for the baseline design, while it is minimized by the design with non-identical tubes. At location C, the identical and non-identical tubes have similar peak velocity magnitudes which are lower than that estimated for the baseline geometry. The trend in the pressure drop across the tube bundle is the same for all the designs: the pressure drop is highest between locations A and B, and lowest between locations D and E. At locations D and E, the local gauge pressure values are negative, and the pressure recovery occurs after location E. The same consideration is applied to the temperature profiles as shown in Fig. 13. The temperature rise across the tube ranks is nearly identical for all the designs implying that the average heat transfer coefficient does not change significantly with tube shape as the heat transfer rate is constrained.

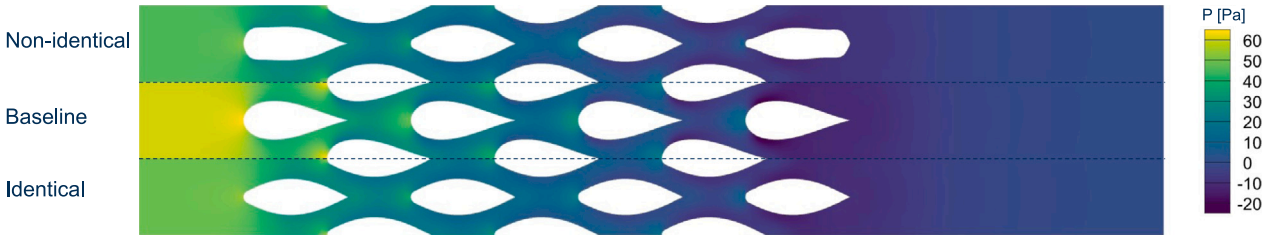

(a) Pressure contours

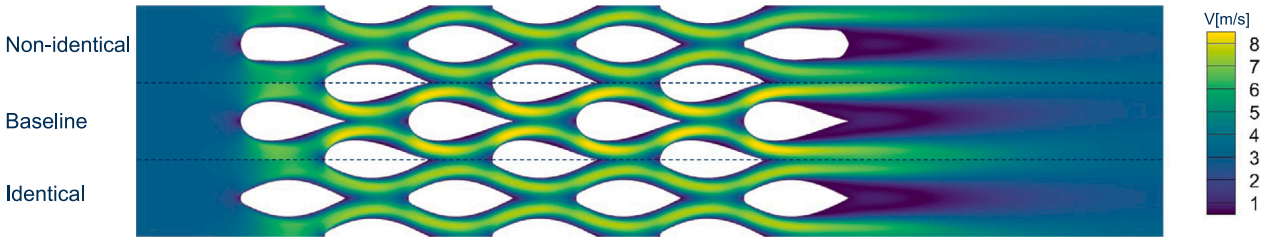

(b) Velocity contours

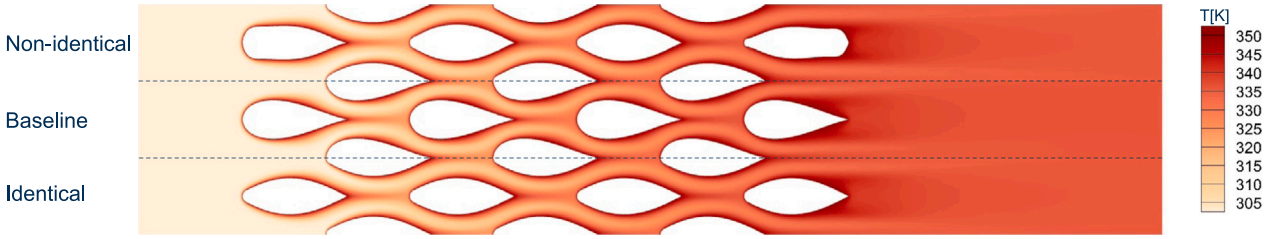

(c) Temperature contours

Fig. 12. Comparison of pressure, velocity, and temperature fields between the baseline design and optimum designs with identical and non-identical tubes.

The distribution of the pressure coefficient (C_p) and the heat flux (q'') on the surfaces of different tubes is displayed in Fig. 14. The C_p distribution for the baseline design reveals a sharp drop of this quantity near the leading edge followed by a limited recovery, thus indicating that the region of adverse pressure gradient and flow deceleration extends till the rear-end of the tube. Conversely, for the optimum designs, the C_p decreases smoothly and stays relatively constant in the second half of tubes 3, 5, and 7. Tube 1 of the solution with non-identical tubes exhibits a sharper decrease in C_p at the leading edge than the identical tube, but the extent of the region with adverse pressure gradient is much smaller, resulting in lower drag forces. The heat flux for the optimum designs at tubes 3 and 5 exhibits overlapping distribution. In the case of tube 1, the average heat flux is the highest for the optimum solution with identical tubes, while for tube 7, the non-identical design results in higher heat flux values, though the difference in heat flux remains small.

4.3. Entropy generation analysis

To further compare the optimum designs, the fluid-dynamic performance of the different HEX configurations is characterized by performing a loss breakdown analysis based on entropy generation. The change of entropy along the flow path occurs because of irreversible processes associated with viscous dissipation and heat transfer across finite temperature differences, as well as due to reversible heat transfer. The total rate of entropy generation across an arbitrarily defined control volume can therefore be written as

$$\dot{S}_{\text{total}} = \dot{S}_{\text{irr}} + \dot{S}_{\text{rev}}. \tag{10}$$

The rate of irreversible entropy generation is the result of two contributions: the first one ($\dot{S}_{\text{irr-ht}}$) due to the fact that the heat transfer occurs over a finite temperature difference, and the second one due to viscous stresses ($\dot{S}_{\text{visc}}$). Therefore, the irreversible entropy generation can be written as

$$\dot{S}_{\text{irr}} = \dot{S}_{\text{irr-ht}} + \dot{S}_{\text{visc}}. \tag{11}$$

These two terms can be estimated for a two-dimensional flow field using the following equations [57],

$$\dot{S}'''_{\text{irr-ht}} = \frac{k}{T^2}\left[\left(\frac{\partial T}{\partial x}\right)^2 + \left(\frac{\partial T}{\partial y}\right)^2\right], \tag{12}$$

$$\dot{S}'''_{\text{visc}} = \frac{2\mu}{T}\left[\left(\frac{\partial u}{\partial x}\right)^2 + \left(\frac{\partial v}{\partial y}\right)^2 + \frac{1}{2}\left(\frac{\partial u}{\partial y} + \frac{\partial v}{\partial x}\right)^2\right], \tag{13}$$

where $\dot{S}'''$ indicates the volumetric rate of entropy generation, k is the effective thermal conductivity, μ is the effective dynamic viscosity, T is the temperature and (u, v) are the x,y components of velocity. The rate of entropy generation $\dot{S}$ is computed by integrating $\dot{S}'''$ over the control volume of interest. This integration is performed by multiplying local $\dot{S}'''$ values by their corresponding mesh element areas and summing across the entire control volume, considering unit length in the z-direction.

The analysis of entropy generation across the tube bundle provides insight into the loss mechanisms occurring in the flow, the location of the highest irreversibilities, as well as the impact of shape optimization on their reduction. The rate of irreversible entropy generated in the computational domain for the three cases, estimated according to Eqs. (12) and (13), are tabulated in Table 5. As can be seen from

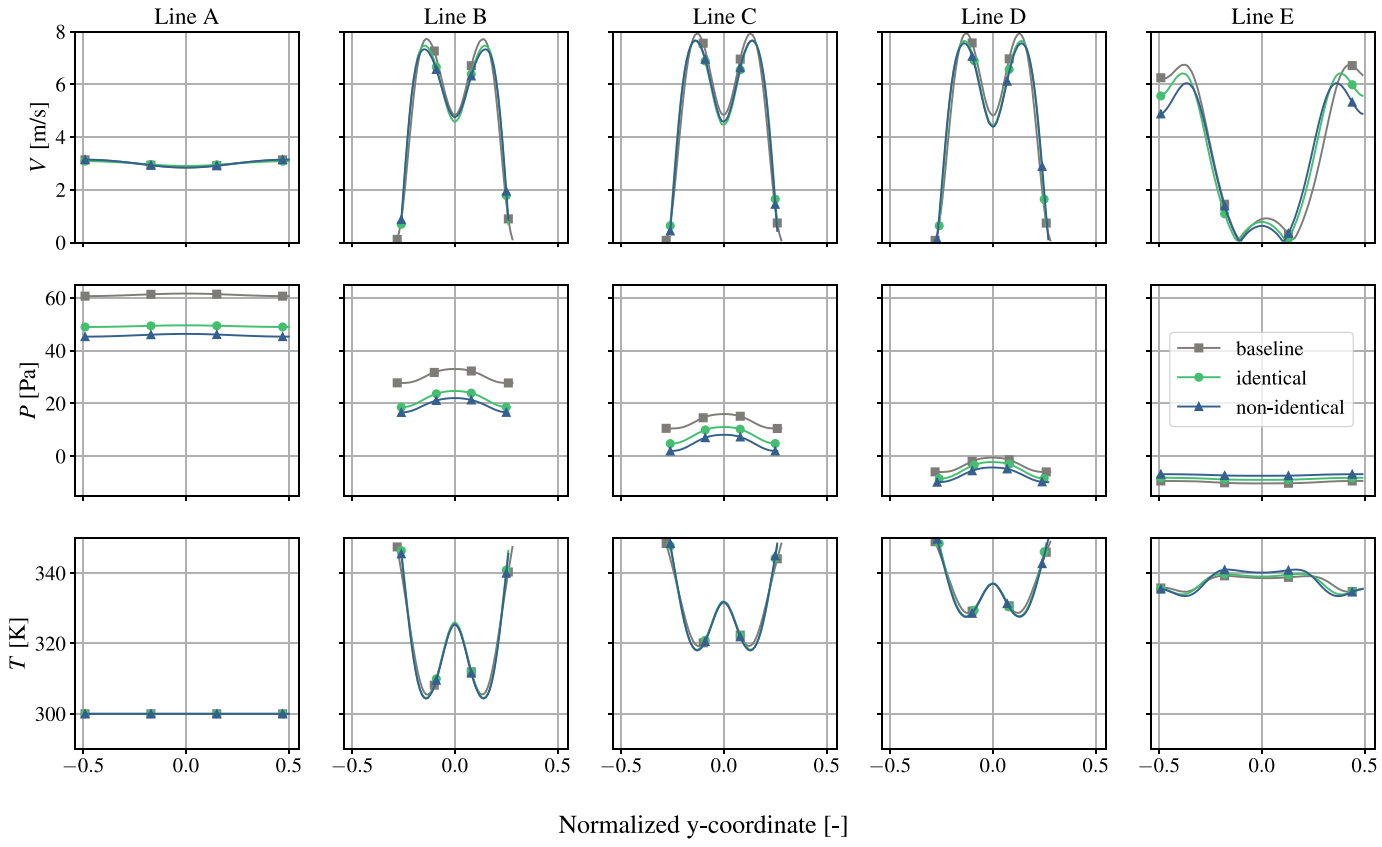

Fig. 13. Variation of flow properties at different locations (A-E) in the flow domain.

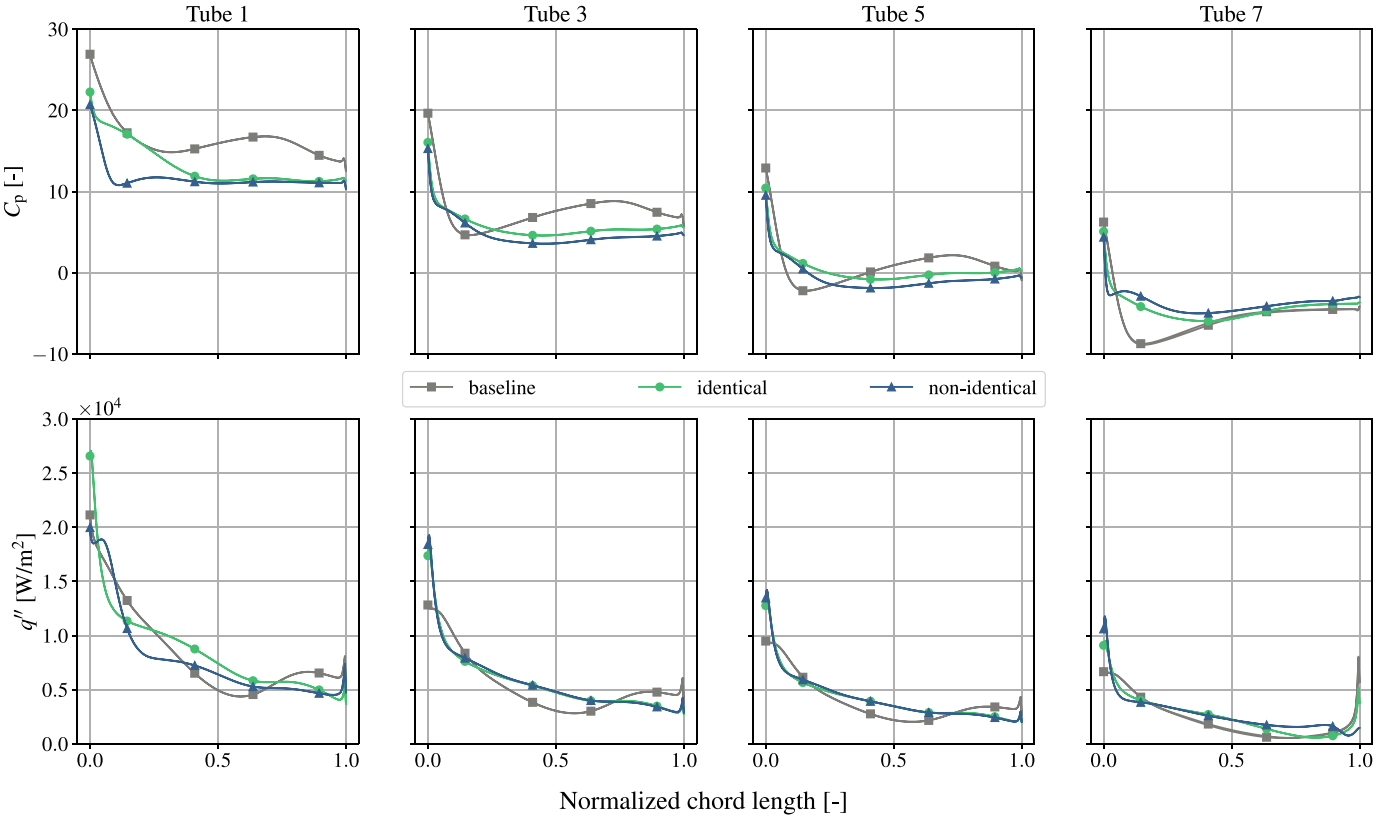

Fig. 14. Comparison of the variation of pressure coefficient and heat flux on tube surfaces between the baseline design and the optimum designs.

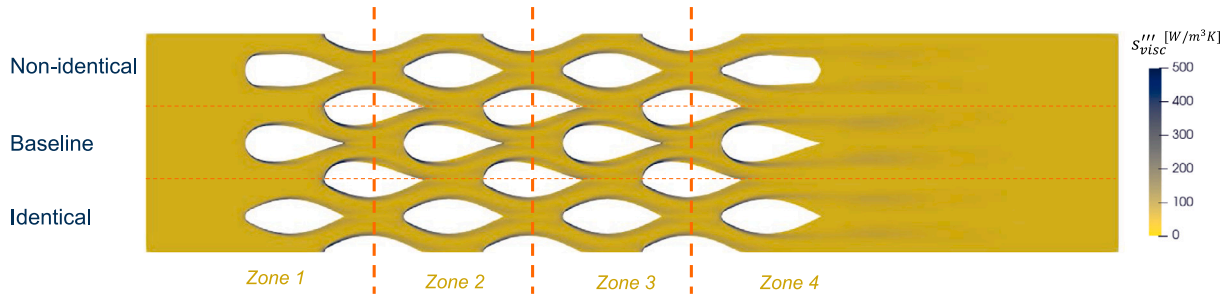

Fig. 15. Volumetric entropy generation rate due to viscous dissipation and subdivision of the flow domain in the four zones used to analyze the irreversible entropy generation along the airflow path.

Table 5
Irreversible entropy generation in the flow solution of the three designs due to heat transfer and viscous stresses.

Case	$\dot{S}_{\mathrm{irr,ht}}$ [W/K]	$\dot{S}_{\mathrm{irr,visc}}$ [W/K]
Baseline	7.761×10^{-2}	1.158×10^{-3}
Identical	7.727×10^{-2}	9.371×10^{-4}
Non-identical	7.712×10^{-2}	8.699×10^{-4}

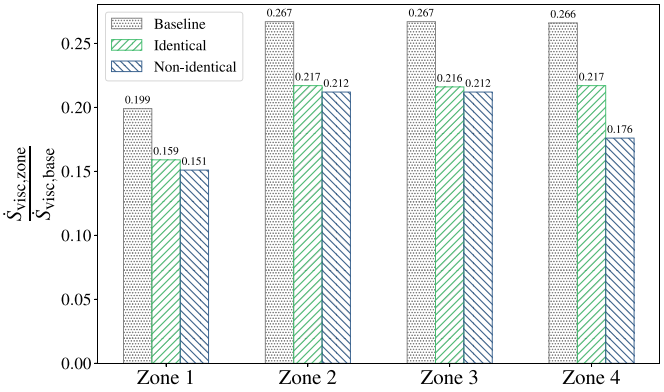

Fig. 16. Zone-wise irreversible entropy generation due to viscous stresses normalized with respect to one in the entire computational domain for the baseline case.

the table, the difference in $\dot{S}_{\mathrm{irr-ht}}$ between the baseline design and the optimum designs is less than 0.75%. This is because the heat transfer does not vary significantly among the design solutions, being constrained to the baseline value in the definition of the optimization problem. However, there is a significant difference in the $\dot{S}_{\mathrm{visc}}$ values. For the solution with identical optimum tubes, the entropy generation rate due to viscous dissipation is about 19% lower than that for the baseline, while for the non-identical case, the decrease is almost 25%. The obtained reductions are proportional to the differences in the pressure drop values.

Fig. 15 shows the contour of the rate of entropy generation due to viscous stresses ($\dot{S}'''_{\mathrm{visc}}$) for the three designs. Higher values of $\dot{S}'''_{\mathrm{visc}}$ are observed within boundary layers in proximity of the regions where the flow acceleration is higher. This is especially visible in the region following the leading edges of the tubes. Additionally, the interface between the free stream and the wake features a higher rate of entropy generation, indicating mixing losses. To analyze the irreversible entropy increase along the flow path and the impact of each tube on loss generation, the computational domain is divided into four zones, as shown in Fig. 15.

The results are shown in the bar chart of Fig. 16. The rate of entropy generation due to viscous effects in each zone ($\dot{S}_{\mathrm{visc,zone}}$) and for each design is normalized with respect to the overall entropy generation rate due to viscous shear computed for the baseline case ($\dot{S}_{\mathrm{visc,base}}$). The optimized tube geometries minimize the entropy generation rate in each zone. In Zone 2 and Zone 3, there is no appreciable difference in the reduction of entropy generation for the optimal case with non-identical tubes versus the one with identical tubes. In Zone 1, the entropy generation rate for the optimum configuration with identical tubes is 20% lower compared to the baseline geometry, and 24% lower for that with non-identical tubes. Most of the decrease in entropy generation is attributed to the change of shape of the last tube. The reduction in entropy generation rate is, respectively, 18.4% and 33.8% compared to the baseline case. From these findings, it can be concluded that an adjoint-based optimization method, enabling the simultaneous and independent optimization of bare tubes, can lead to heat exchangers with significantly better thermal-hydraulic performance.

5. Conclusions

The objective of this work was to propose a method to perform adjoint-based shape optimization of multiple heat transfer surfaces represented with a CAD-based parametrization. For this purpose, an automated design chain, consisting of the open-source CFD suite SU2 [38] and NURBS-based CAD parametrization [37], and implemented in a python-based framework, was applied to an exemplary bare-tube heat exchanger. Using such a design chain, multiple heat transfer surfaces were optimized concurrently with the objective of reducing air-side pressure drop while constraining the heat transfer rate and the tube cross-section internal areas. Two variations of the optimization problem are investigated in the study: one utilizing averaged sensitivities and the other utilizing local sensitivities, resulting in an optimum solution with identical and non-identical tube shapes, respectively.

The conclusions from the research presented in this manuscript are as follows:

1. Optimum designs were obtained with 11 and 19 design iterations for the case with identical and non-identical tubes, respectively. The case with identical tubes leads to a faster optimization convergence due to fewer distinct design variables as a result of the sensitivity averaging.
2. The performance improvements for the cases with identical and non-identical tubes were 19.41% and 25.05% respectively. In the case of non-identical tubes, the first and the last tube in the streamwise direction exhibited a large difference in shape to optimize the flow cross-sectional area variation along the streamwise direction, thus leading to a smoother flow acceleration.
3. Zone-wise entropy generation analysis demonstrated that using the second law of thermodynamics helps identify the effect of individual tube shapes on performance improvement. The entropy generation due to viscous dissipation in Zone 4, containing the last full tube in the computational domain, was for the cases of identical and non-identical tubes 18.4% and 33.8% lower than the baseline, respectively.

Overall, using the proposed method, concurrent optimization of tubular HEX using local sensitivities, resulting in non-identical tube shapes, leads to higher design improvement when compared to identical shapes, with limited impact on the computation cost.

A key challenge faced in this study involving many design variables in the optimization process was linked with large mesh deformations in the intermediate design evaluations. One approach to tackle this challenge was setting appropriate bounds on design variables. Moreover, the mesh quality resulting from large mesh deformations is an important aspect that needs to be considered in future studies. Additionally, the layout of the tubes was kept fixed, so the effect of the tube bundle configuration on heat exchanger performance was not investigated in this study.

Future work will focus on simulating conjugate heat transfer for 3D shape optimization with CAD-based parametrization of heat transfer surfaces.

CRediT authorship contribution statement

Praharsh Pai Raikar: Writing – original draft, Methodology, Investigation, Funding acquisition, Conceptualization. **Nitish Anand:** Writing – review & editing, Supervision, Methodology, Conceptualization. **Matteo Pini:** Writing – review & editing, Supervision, Methodology, Conceptualization. **Carlo De Servi:** Writing – review & editing, Supervision, Methodology, Funding acquisition, Conceptualization.

Declaration of competing interest

Carlo De Servi, Praharsh Pai Raikar, and Nitish Anand have patent #EP23216416.0 pending to VITO NV. The authors have patent #EP23216402.0 pending to VITO NV and Delft University of Technology. The authors declare that they have no known additional competing financial interests or personal relationships that could have appeared to influence the work reported in this paper.

Data availability

Data will be made available on request.

Acknowledgments

The research reported in this manuscript was funded by the Vlaamse Instelling voor Technologisch Onderzoek (VITO), Belgium, through project number 2010489. The authors are also grateful to Prof. P. Colonna for his valuable comments during the development of this study.

References

[1] S. Kaiser, O. Schmitz, P. Ziegler, H. Klingels, The water-enhanced turbofan as enabler for climate-neutral aviation, Appl. Sci. 12 (23) (2022) http://dx.doi.org/10.3390/app122312431.

[2] M. Hughes, J. Olsen, Fuel burn reduction of hybrid aircraft employing an exhaust heat harvesting system, J. Propuls. Power 38 (2) (2022) 241–253, http://dx.doi.org/10.2514/1.B38393.

[3] B. Sundén, J. Fu, Chapter 6 - Aerospace heat exchangers, in: B. Sundén, J. Fu (Eds.), Heat Transfer in Aerospace Applications, Academic Press, 2017, pp. 89–115, http://dx.doi.org/10.1016/B978-0-12-809760-1.00006-5.

[4] R.K. Shah, D.P. Sekulic, Overview of heat exchanger design methodology, in: Fundamentals of Heat Exchanger Design, John Wiley & Sons, Ltd, 2003, pp. 78–96, http://dx.doi.org/10.1002/9780470172605.ch2, Ch. 2.

[5] M. Ahmadian-Elmi, A. Mashayekhi, S.S. Nourazar, K. Vafai, A comprehensive study on parametric optimization of the pin-fin heat sink to improve its thermal and hydraulic characteristics, Int. J. Heat Mass Transfer 180 (2021) 121797, http://dx.doi.org/10.1016/j.ijheatmasstransfer.2021.121797.

[6] N. Tran, C.C. Wang, Effects of tube shapes on the performance of recuperative and regenerative heat exchangers, Energy 169 (2019) 1–17, http://dx.doi.org/10.1016/j.energy.2018.11.127.

[7] A. Sadeghianjahromi, C.C. Wang, Heat transfer enhancement in fin-and-tube heat exchangers – A review on different mechanisms, Renew. Sustain. Energy Rev. 137 (2021) 110470, http://dx.doi.org/10.1016/j.rser.2020.110470.

[8] L. Zhao, X. Gu, L. Gao, Z. Yang, Numerical study on airside thermal-hydraulic performance of rectangular finned elliptical tube heat exchanger with large row number in turbulent flow regime, Int. J. Heat Mass Transfer 114 (2017) 1314–1330, http://dx.doi.org/10.1016/j.ijheatmasstransfer.2017.06.049.

[9] W. Xi, J. Cai, X. Huai, Numerical investigation on fluid-solid coupled heat transfer with variable properties in cross-wavy channels using half-wall thickness multi-periodic boundary conditions, Int. J. Heat Mass Transfer 122 (2018) 1040–1052, http://dx.doi.org/10.1016/j.ijheatmasstransfer.2018.02.055.

[10] N. Tran, Y. Chang, J. Teng, R. Greif, A study on five different channel shapes using a novel scheme for meshing and a structure of a multi-nozzle microchannel heat sink, Int. J. Heat Mass Transfer 105 (2017) 429–442, http://dx.doi.org/10.1016/j.ijheatmasstransfer.2016.09.076.

[11] N. Tran, J. Liaw, C. Wang, Performance of thermofluidic characteristics of recuperative wavy-plate heat exchangers, Int. J. Heat Mass Transfer 170 (2021) 121027, http://dx.doi.org/10.1016/j.ijheatmasstransfer.2021.121027.

[12] X. Li, D. Zhu, Y. Yin, A. Tu, S. Liu, Parametric study on heat transfer and pressure drop of twisted oval tube bundle with in line layout, Int. J. Heat Mass Transfer 135 (2019) 860–872, http://dx.doi.org/10.1016/j.ijheatmasstransfer.2019.02.031.

[13] P. Ranut, G. Janiga, E. Nobile, D. Thévenin, Multi-objective shape optimization of a tube bundle in cross-flow, Int. J. Heat Mass Transfer 68 (2014) 585–598, http://dx.doi.org/10.1016/j.ijheatmasstransfer.2013.09.062.

[14] S. Patankar, C. Liu, E.M. Sparrow, Fully developed flow and heat transfer in ducts having streamwise-periodic variations of cross-sectional area, J. Heat Transfer 99 (1977) 180–187, http://dx.doi.org/10.1115/1.3450666.

[15] D. Bacellar, V. Aute, Z. Huang, R. Radermacher, Design optimization and validation of high-performance heat exchangers using approximation assisted optimization and additive manufacturing, Sci. Technol. Build Environ. 23 (6) (2017) 896–911, http://dx.doi.org/10.1080/23744731.2017.1333877.

[16] H. Lim, U. Han, H. Lee, Design optimization of bare tube heat exchanger for the application to mobile air conditioning systems, Appl. Therm. Eng. 165 (2020) 114609, http://dx.doi.org/10.1016/j.applthermaleng.2019.114609.

[17] H. Kang, U. Han, H. Lim, H. Lee, Y. Hwang, Numerical investigation and design optimization of a novel polymer heat exchanger with ogive sinusoidal wavy tube, Int. J. Heat Mass Transfer 166 (2021) 120785, http://dx.doi.org/10.1016/j.ijheatmasstransfer.2020.120785.

[18] J. Tancabel, V. Aute, E. Klein, C.Y. Lee, Y. Hwang, J. Ling, J. Muehlbauer, R. Radermacher, Multi-scale and multi-physics analysis, design optimization, and experimental validation of heat exchangers utilizing high performance, non-round tubes, Appl. Therm. Eng. 216 (2022) 118965, http://dx.doi.org/10.1016/j.applthermaleng.2022.118965.

[19] J. Wen, H. Yang, G. Jian, X. Tong, K. Li, S. Wang, Energy and cost optimization of shell and tube heat exchanger with helical baffles using Kriging metamodel based on MOGA, Int. J. Heat Mass Transfer 98 (2016) 29–39, http://dx.doi.org/10.1016/j.ijheatmasstransfer.2016.02.084.

[20] C. Liu, W. Bu, D. Xu, Multi-objective shape optimization of a plate-fin heat exchanger using CFD and multi-objective genetic algorithm, Int. J. Heat Mass Transfer 111 (2017) 65–82, http://dx.doi.org/10.1016/j.ijheatmasstransfer.2017.03.066.

[21] X. Wang, N. Zheng, Z. Liu, W. Liu, Numerical analysis and optimization study on shell-side performances of a shell and tube heat exchanger with staggered baffles, Int. J. Heat Mass Transfer 124 (2018) 247–259, http://dx.doi.org/10.1016/j.ijheatmasstransfer.2018.03.081.

[22] G.W. Mann, S. Eckels, Multi-objective heat transfer optimization of 2D helical micro-fins using NSGA-II, Int. J. Heat Mass Transfer 132 (2019) 1250–1261, http://dx.doi.org/10.1016/j.ijheatmasstransfer.2018.12.078.

[23] S. Soleimani, S. Eckels, Multi-objective optimization of 3D micro-fins using NSGA-II, Int. J. Heat Mass Transfer 197 (2022) 123315, http://dx.doi.org/10.1016/j.ijheatmasstransfer.2022.123315.

[24] K. Hu, C. Lu, B. Yu, L. Yang, Y. Rao, Optimization of bionic heat sinks with self-organized structures inspired by termite nest morphologies, Int. J. Heat Mass Transfer 202 (2023) 123735, http://dx.doi.org/10.1016/j.ijheatmasstransfer.2022.123735.

[25] Y.A. Manaserh, A.R. Gharaibeh, M.I. Tradat, S. Rangarajan, B.G. Sammakia, H.A. Alissa, Multi-objective optimization of 3D printed liquid cooled heat sink with guide vanes for targeting hotspots in high heat flux electronics, Int. J. Heat Mass Transfer 184 (2022) 122287, http://dx.doi.org/10.1016/j.ijheatmasstransfer.2021.122287.

[26] M.E. Polat, S. Cadirci, Artificial neural network model and multi-objective optimization of microchannel heat sinks with diamond-shaped pin fins, Int. J. Heat Mass Transfer 194 (2022) 123015, http://dx.doi.org/10.1016/j.ijheatmasstransfer.2022.123015.

[27] J. Nocedal, S.J. Wright, Numerical optimization, second ed., Springer Series in Operations Research and Financial Engineering, Springer, New York, 2006, http://dx.doi.org/10.1007/978-0-387-40065-5.

[28] R. Zhang, X. Qian, Parameter-free shape optimization of heat sinks, in: Proceedings of InterSociety Conference on Thermal and Thermomechanical Phenomena in Electronic Systems, ITherm, 2020, pp. 756–765, http://dx.doi.org/10.1109/ITherm45881.2020.9190501.
[29] K. Wang, X.Y. Zhang, Z.D. Zhang, C.H. Min, Three-dimensional shape optimization of fins in a printed circuit recuperator using S-CO2 as the heat-transfer fluid, Int. J. Heat Mass Transfer 192 (2022) 122910, http://dx.doi.org/10.1016/j.ijheatmasstransfer.2022.122910.
[30] J.L. Anibal, C.A. Mader, J.R. Martins, Aerodynamic shape optimization of an electric aircraft motor surface heat exchanger with conjugate heat transfer constraint, Int. J. Heat Mass Transfer 189 (2022) 122689, http://dx.doi.org/10.1016/j.ijheatmasstransfer.2022.122689.
[31] J.L. Anibal, J.R. Martins, Adjoint-based shape optimization of a plate-fin heat exchanger using CFD, Appl. Therm. Eng. 252 (2024) 123570, http://dx.doi.org/10.1016/j.applthermaleng.2024.123570.
[32] K.T. Gkaragkounis, E.M. Papoutsis-Kiachagias, K.C. Giannakoglou, Adjoint-assisted Pareto front tracing in aerodynamic and conjugate heat transfer shape optimization, Comput. & Fluids 214 (2021) 104753, http://dx.doi.org/10.1016/j.compfluid.2020.104753.
[33] S. Vitale, M. Pini, P. Colonna, Multistage turbomachinery design using the discrete adjoint method within the open-source software SU2, J. Propuls. Power 36 (3) (2020) 465–478, http://dx.doi.org/10.2514/1.B37685.
[34] L. Mueller, T. Verstraete, CAD integrated multipoint adjoint-based optimization of a turbocharger radial turbine, Int. J. Turbomach. Propuls. Power 2 (3) (2017) http://dx.doi.org/10.3390/ijtpp2030014.
[35] N. Anand, S. Vitale, M. Pini, P. Colonna, Assessment of FFD and CAD-based shape parametrization methods for adjoint-based turbomachinery shape optimization, in: Proceedings of Global Power and Propulsion Society, Montreal, Canada, 2018, pp. 1–8, http://dx.doi.org/10.5281/zenodo.1344595.
[36] S. Xu, D. Radford, M. Meyer, J.-D. Müller, CAD-based adjoint shape optimisation of a one-stage turbine with geometric constraints, in: Proceeding of Turbo Expo: Power for Land, Sea, and Air, Vol. Volume 2C: Turbomachinery, 2015, V02CT45A006, http://dx.doi.org/10.1115/GT2015-42237.
[37] R. Agromayor, N. Anand, J.D. Muller, M. Pini, L.O. Nord, A unified geometry parametrization method for turbomachinery blades, Comput. Aided Des. 133 (102987) (2021) 1–16, http://dx.doi.org/10.1016/j.cad.2020.102987.
[38] T.D. Economon, F. Palacios, S.R. Copeland, T.W. Lukaczyk, J.J. Alonso, SU2: An open-source suite for multiphysics simulation and design, AIAA J. 54 (3) (2016) 828–846, http://dx.doi.org/10.2514/1.J053813.
[39] R. Agromayor, N. Anand, M. Pini, L.O. Nord, Multirow adjoint-based optimization of NICFD turbomachinery using a computer-aided design-based parametrization, J. Eng. Gas Turbines Power 144 (4) (2022) http://dx.doi.org/10.1115/1.4052881.
[40] A. Châtel, T. Verstraete, Multidisciplinary optimization of the SRV2-O radial compressor using an adjoint-based approach, Struct. Multidiscip. Optim. 66 (5) (2023) 1–13, http://dx.doi.org/10.1007/s00158-023-03556-2.
[41] K. Gkaragkounis, E. Papoutsis-Kiachagias, K. Giannakoglou, The continuous adjoint method for shape optimization in Conjugate Heat Transfer problems with turbulent incompressible flows, Appl. Therm. Eng. 140 (2018) 351–362.
[42] Various Authors, Parablade, 2020, http://dx.doi.org/10.5281/zenodo.3894778.
[43] P.E. Gill, W. Murray, M.A. Saunders, SNOPT: An SQP algorithm for large-scale constrained optimization, SIAM Rev. 47 (1) (2005) 99–131, http://dx.doi.org/10.1137/S0036144504446096.
[44] N. Wu, G. Kenway, C.A. Mader, J. Jasa, J.R.R.A. Martins, PyOptSparse: A python framework for large-scale constrained nonlinear optimization of sparse systems, J. Open Source Softw. 5 (54) (2020) 2564, http://dx.doi.org/10.21105/joss.02564.
[45] W. Squire, G. Trapp, Using complex variables to estimate derivatives of real functions, SIAM Rev. 40 (1) (1998) 110–112, http://dx.doi.org/10.1137/S003614459631241X.
[46] R. Dwight, Robust mesh deformation using the linear elasticity equations, in: Computational Fluid Dynamics 2006, 2009, pp. 401–406, http://dx.doi.org/10.1007/978-3-540-92779-2_62.
[47] T.D. Economon, Simulation and adjoint-based design for variable density incompressible flows with heat transfer, AIAA J. 58 (2) (2020) 757–769, http://dx.doi.org/10.2514/1.J058222.
[48] E.F. Toro, Flux vector splitting methods, in: Riemann Solvers and Numerical Methods for Fluid Dynamics: A Practical Introduction, Springer Berlin Heidelberg, 1997, pp. 249–271, http://dx.doi.org/10.1007/978-3-662-03490-3_8, Ch. 8.
[49] B. van Leer, Towards the ultimate conservative difference scheme. V. A second-order sequel to Godunov's method, J. Comput. Phys. 32 (1) (1979) 101–136, http://dx.doi.org/10.1016/0021-9991(79)90145-1.
[50] J. Blazek, Computational Fluid Dynamics: Principles and Applications, third ed., Butterworth-Heinemann, Oxford, 2015, pp. 163–165, http://dx.doi.org/10.1016/B978-0-08-099995-1.00005-1.
[51] P.R. Spalart, S.R. Allmaras, A one-equation turbulence model for aerodynamic flows, in: Proceedings of 30th Aerospace Sciences Meeting and Exhibit, 1992, pp. 5–21, http://dx.doi.org/10.2514/6.1992-439.
[52] Y. Saad, Iterative Methods for Sparse Linear Systems, second ed., Society for Industrial and Applied Mathematics, 2003, http://dx.doi.org/10.1137/1.9780898718003.
[53] M. Sagebaum, T. Albring, N.R. Gauger, High-performance derivative computations using CoDiPack, ACM Trans. Math. Software 45 (4) (2019) http://dx.doi.org/10.1145/3356900.
[54] T.A. Albring, M. Sagebaum, N.R. Gauger, Efficient aerodynamic design using the discrete adjoint method in SU2, in: Proceedings of 17th AIAA/ISSMO Multidisciplinary Analysis and Optimization Conference, AIAA, 2016, pp. 1–15, http://dx.doi.org/10.2514/6.2016-3518.
[55] I. Pointwise, Pointwise, 2022, [Computer software], https://www.pointwise.com.
[56] B. Braden, The surveyor's area formula, College Math. J. 17 (4) (1986) 326–337, http://dx.doi.org/10.1080/07468342.1986.11972974.
[57] A. Bejan, The thermodynamic design of heat and mass transfer processes and devices, Int. J. Heat Fluid Flow 8 (4) (1987) 258–276, http://dx.doi.org/10.1016/0142-727X(87)90062-2.